Available online at www.sciencedirect.com
SCIENCE DIRECT®
Icarus 170 (2004) 193–201
ICARUS
www.elsevier.com/locate/icarus

# Ice–silicate fractionation among icy bodies due to the difference of impact strength between ice and ice–silicate mixture

Masahiko Arakawa * and Daisuke Tomizuka

*Institute of Low Temperature Science, Hokkaido University, Kita-Ku Kita 19 Nishi 8, Sapporo 060-0819, Japan*

Received 18 August 2003; revised 9 February 2004

Available online 9 April 2004

**Abstract**

Laboratory experiments on the impact disruption of ice–silicate mixtures were conducted to clarify the accretion process of small icy bodies. Since the icy bodies are composed of ice and silicates with various porosities, we investigated the effect of porosity on the impact disruption of mixtures. We tested the mixture target with the mass ratio of ice to silicate, 0.5 and with 5 different porosities (0, 12.5, 25, 32, 37%) at the impact velocities of 150 to 670 m/s. The silicate mass ratio was changed from 0 to 0.5 in steps of 0.1 at a porosity of 12.5% and a constant impact velocity of about 300 m/s. The impact strength of the mixture was found to decrease with increasing porosity and the silicate mass ratio between 0.1 and 0.5 could enhance the strength of the icy target. The observed dependence of the impact strength on the porosity is opposite to that observed for pure ice. This difference could play an important role in ice–silicate fractionation during the accretion process. Because, ice rich bodies are easily broken as the porosity decreases in their evolution, the collisional growth could be prohibited. On the other hand, among the silicate rich bodies the collisional growth could be enhanced.


*Keywords:* Accretion; Cratering; Ices; Impact processes; Satellites, general

## 1. Introduction

There are a lot of icy bodies found in outer Solar System. The number of the bodies continues to increase with the discovery of icy satellites (e.g., Gladman et al., 1998, 2000, 2001) and Kuiper belt objects (e.g., Jewitt, 1999; Luu and Jewitt, 2002). The varieties of icy bodies are quite remarkable: there are wide ranges of sizes, densities and surface geologies among them. Saturn is the best representative of a satellite system with icy bodies orbiting. It has one large satellite, Titan, several middle size satellites (e.g., Rhea, Iapetus, Dione, Tethys), and rings. The formation process of this satellite system is unclear though there are some working hypotheses (Coradini et al., 1989).

It is well known that the density of Titan, 1.88 g/cm$^3$, is considerably larger than other smaller icy satellites (1.2–1.4 g/cm$^3$). This apparent difference in the densities may result from phase transitions of water ice to high-density phases in Titan's interior (Lupo and Lewis, 1979) or from the silicate fractionation during the accretion process (Ahrens and O'Keefe, 1985). However these hypotheses are based on the assumption that satellitesimals in a subnebula around Saturn were homogeneous in their compositions. Other models of subnebula adopt a temperature distribution with distance and time (Canup and Ward, 2002; Mosqueria and Estrada, 2003a, 2003b; Lunine and Stevenson, 1982). According to these models, the chemical composition of the subnebula should be heterogeneous in the volatile elements: however the relative ratio of water ice to silicates in solid could be changed with the distance from the central planet. If so, we can consider the possibility that the satellite system was formed through the collisional accretion among the small icy bodies with the different silicate contents from the beginning. Therefore it is worthwhile to evaluate the effect of silicate contents on accretion in high velocity impacts. The minimum collisional velocity among icy satellites can be estimated by calculating their escape velocities, e.g., 2640 m/s for Titan and 160 m/s for Mimas.

Recent evidence indicates many asteroids have high porosity (Britt and Consolmagno, 2001). Therefore, porosity has been considered to be a key physical parameter to control the evolutions of small satellites (Housen et al., 1999;

* Corresponding author. Fax: +81-11-706-7142.
*E-mail address:* arak@lowtem.hokudai.ac.jp (M. Arakawa).

0019-1035/$ – see front matter 
doi:10.1016/j.icarus.2004.02.009

Housen and Holsapple, 2003). Arakawa et al. (2002) systematically studied the impact strength of water ice with various porosities from 0 to 55% and found that the strength increases rapidly with increasing porosity. The characteristics that the porosity strengthens the material against the impact are also found in crushed ice aggregates (Ryan et al., 1999), gypsum and clay (Davis and Ryan, 1990), and sintered glass particles (Love et al., 1993). However, if icy satellites are assumed to be mixtures of ice and silicates, it is necessary to study the effect of silicate/ice ratio at various porosities. The dynamic tensile strength of ice–silicate mixture was measured by Lange and Ahrens (1983) for the silicate contents of 5 and 30 wt%. These non-porous mixtures were observed to have tensile strength of $\sim 20$ and 22 MPa, respectively. In our previous study (Arakawa et al., 2002), one series of impact experiments (7 runs) was carried out for ice–pyrophyllite mixtures with a porosity of 38%. Very limited experiments (only 3 runs) were carried out for the target with 3 different porosities as a pilot test. We found that the impact strength of the mixture with the porosity of 38% was almost the same as that of pure ice. However these pilot tests also found a very curious result in that the impact strength increased with decreasing porosity. We speculated that the impact strength of the mixture had the opposite porosity dependence of pure ice. The theoretical consideration to explain this curious feature was conducted according to the framework proposed by Mizutani et al. (1990). Consequently, we pointed out that the porosity dependencies of the static mechanical strength and the shock pressure attenuation were keys to solve this problem. Therefore, in this following study, we conducted a complete series of impact experiments (32 runs) for ice–silicate mixtures with 5 different porosities (0, 12.5, 25, 32, 37%) in order to understand how porosity affects impact strength and to study the effect of physical properties of silicate materials on the strength. We also carried out preliminary experiments to study the effect of silicate contents on the impact strength of porous icy targets with a constant porosity at a constant impact velocity. In addition to these impact experiments, the static mechanical tests for pure ice and ice–silicate mixture were carried out to examine the relationship between the porosity and mechanical strength.

## 2. Experimental method

The impact experiments used a vertical He-gas gun set in a large cold room of our laboratory at a normal temperature of $-10\,^{\circ}$C. The experimental details were the same as that described in Arakawa et al. (2002), so we describe the method only briefly here. The ice projectiles had a mass of 1.6 g, were cylindrical in shape (15 mm diameter, 10 mm height) was launched at impact velocities ($v_i$) from 150 to 670 m/s normal to the target surface (Table 1). The projectile impacted the center of the target surface (head on collision). The targets (except for the non-porous target) were cylinders with 7 cm diameter and 7 cm height (see Table 1, *Misc*. for the non-porous target). The target was a mixture of water ice powder and micron sized serpentine powder ($<$ several μm). Our previous study used pyrophyllite powder for the silicate material (Arakawa et al., 2002), whose grain size ($\sim 10$ μm) was larger than that of the serpentine powder used in this study. It should also be noted that there are several differences between the physical properties of pyrophyllite and serpentine, e.g., density, bulk sound velocity, and static strength (2711 kg/m$^3$, 3000 m/s, 73 MPa for pyrophyllite and 2621 kg/m$^3$, 5300 m/s, 137 MPa for serpentine, respectively). The ice powder was prepared by crushing a commercial ice block using an electric mixer. The crushed ice was sieved to leave only particles less than 500 μm. They were mixed in the weight ratio of 50:50, i.e., a silicate content of $C = 0.5$. The target had 5 different porosities ($\phi$), 0, 12.5, 25, 32, and 37%. The mixture sample was compressed at $-10\,^{\circ}$C. Pressure sintering was used to regulate target porosity. The non-porous sample was made by gradually freezing the mixed powder filled with liquid water. We also prepared the mixture with various silicate contents of $C = 0.1$, 0.2, 0.3, 0.4 for the constant porosity of 12.5%.

The target was set in an acrylic box to recover the impact fragments. The mass distribution was observed for each shot to determine the representative fragment mass, $f_{0.5}$, to describe the degree of impact disruption (Arakawa et al., 2002), instead of the widely-used largest fragment mass. This newly proposed parameter provides a valuable description of the degree of impact disruption.

The disrupted fragments and the cratering ejecta were observed by an image-converter camera to determine the maximum fragment velocity. In order to visualize even very fine fragments, a shadow photograph lightening system was used, so that the ejecta looked like a black shadow in the photos (Figs. 1a and 1b). The camera takes 12 successive images every 10 to 100 μs with each exposure time of 800 ns. Since the spatial resolution is not enough to distinguish each fine fragment, we analyze the maximum expansion velocity of the ejecta envelope as the maximum fragment velocity. The maximum ejecta velocity is a key parameter to represent the re-accumulation condition to construct a regolith layer on the bodies (Arakawa et al., 1995; Arakawa and Higa, 1996; Arakawa, 1999).

The static mechanical tests were carried out by using a mechanical testing machine (Tensilon UCT-2.5T, Orientec Corp.) set in a cold room at the temperature of $-10\,^{\circ}$C. The pure ice and mixture samples ($C = 0.5$) with 4 different porosities (12.5, 25, 32, 37%) were prepared by the pressure-sintering method described above. The sample was a cylinder with the diameter of 3 cm and the height of 6 cm. The unconfined compression test at a constant strain rate of $5.6 \times 10^{-3}$ s$^{-1}$ was applied to these samples and the stress strain curves were acquired for each test. The maximum stress was determined in each stress-strain curve and we used this maximum stress as the static strength of these samples.

Table 1
Experimental conditions and results

| Run No. | $M_t$ (g) | $v_i$ (m/s) | $m_l$ (g) | $m_l/M_t$ | $Q$ (J/kg) | $f_{0.5}$ | $v_{e\text{-}max}$ | *Misc.*[a] |
|---|---|---|---|---|---|---|---|---|
| Porosity = 0% | | | | | | | | |
| 830-3 | 247.45 | 156 | 247.31 | 0.999 | 78.2 | n.d. | – | 6.4, 5.3, 6.4 |
| 829-2 | 202.43 | 218 | 159.86 | 0.790 | 184.3 | 0.22 | – | 5.8, 5.2, 6.3 |
| 829-1 | 152.90 | 305 | 20.25 | 0.132 | 471.5 | 0.034 | – | 4.4, 5.3, 6.0 |
| 904-1 | 247.66 | 305 | 183.98 | 0.743 | 296.7 | 0.13 | – | 6.3, 5.4, 6.7 |
| 829-3 | 195.26 | 465 | 12.50 | 0.0640 | 858.2 | 0.011 | – | 5.7, 5.2, 6.3 |
| 830-1 | 204.71 | 554 | 16.20 | 0.0791 | 1161.9 | 0.0056 | – | 5.4, 5.4, 6.5 |
| 830-2 | 246.46 | 651 | 14.43 | 0.0585 | 1341.2 | 0.0066 | – | 6.5, 5.4, 6.4 |
| Porosity = 12.5% | | | | | | | | |
| 708-3 | 315.34 | 155 | 315.08 | 0.999 | 59.9 | n.d. | 229[b] | |
| 708-4 | 315.23 | 217 | 285.22 | 0.905 | 121.0 | 0.32 | 257 | |
| 708-5 | 314.78 | 303 | 188.00 | 0.597 | 236.3 | 0.051 | 256 | |
| 708-6 | 315.44 | 465 | 24.95 | 0.0791 | 545.0 | 0.008 | 488 | |
| 708-7 | 315.44 | 548 | 22.12 | 0.0701 | 756.9 | 0.004 | 528 | |
| 708-8 | 315.03 | 650 | 15.94 | 0.0506 | 1059.5 | 0.0026 | 764 | |
| Porosity = 25% | | | | | | | | |
| 708-1 | 268.89 | 147 | 233.34 | 0.867 | 62.3 | 0.25 | 96 | |
| 704-2 | 270.04 | 209 | 156.98 | 0.581 | 134.3 | 0.11 | 114 | |
| 704-3 | 270.06 | 290 | 130.81 | 0.484 | 249.1 | 0.029 | 161 | |
| 704-4 | 270.08 | 452 | 17.01 | 0.0630 | 586.3 | 0.004 | 262 | |
| 704-5 | 269.37 | 571 | 11.02 | 0.0409 | 938.0 | 0.0021 | 295 | |
| 708-2 | 268.86 | 638 | 11.80 | 0.0439 | 1188.5 | 0.0005 | 309 | |
| Porosity = 32% | | | | | | | | |
| 1029-1 | 245.18 | 142 | 216.66 | 0.884 | 64.6 | 0.37 | 54 | |
| 1028-1 | 245.28 | 203 | 125.77 | 0.513 | 138.6 | 0.04 | 83 | |
| 1028-2 | 245.24 | 307 | 45.35 | 0.185 | 303.6 | 0.0096 | 145 | |
| 1029-1 | 245.04 | 309 | 54.56 | 0.223 | 307.8 | 0.0076 | 117 | |
| 1028-3 | 244.71 | 431 | 9.88 | 0.0404 | 595.9 | 0.00093 | 249 | |
| 1029-3 | 245.27 | 567 | 9.84 | 0.0401 | 1055.2 | 0.0013 | 282 | |
| 1029-4 | 244.77 | 673 | 6.41 | 0.0262 | 1471.1 | 0.000026 | 353 | |
| Porosity = 37% | | | | | | | | |
| 709-1 | 224.97 | 156 | 34.97 | 0.155 | 86.54 | 0.009 | 27 | |
| 709-2 | 225.54 | 211 | 14.29 | 0.0634 | 155.9 | 0.00022 | 37 | |
| 709-3 | 224.44 | 289 | 12.27 | 0.0547 | 295.9 | n.d. | 57 | |
| 710-1 | 225.49 | 436 | 1.74 | 0.00771 | 674.4 | n.d. | 137 | |
| 710-2 | 225.27 | 549 | 0.86 | 0.00382 | 1077.1 | n.d. | 129 | |
| 710-3 | 225.36 | 646 | 1.00 | 0.00444 | 1472.2 | n.d. | 218 | |
| Porosity = 12.5% | | | | | | | | |
| 1030-1 | 230.77 | 273 | 123.53 | 0.535 | 260.1 | 0.025 | 290 | $C = 0.1$ |
| 1030-2 | 246.62 | 302 | 124.08 | 0.503 | 290.3 | 0.044 | 335 | $C = 0.2$ |
| 1030-3 | 266.41 | 293 | 134.44 | 0.504 | 254.6 | 0.046 | 366 | $C = 0.3$ |
| 1030-4 | 289.20 | 291 | 165.82 | 0.574 | 232.8 | 0.077 | 353 | $C = 0.4$ |

$M_t$ target mass, $v_i$ impact velocity, $m_l$ the largest fragment mass, $Q$ the energy density, $v_{e\text{-}max}$ the maximum ejecta velocity.

[a] The shape of the sample with the porosity 0% is a cone truncated on the top, which looks trapezoid on the side view. So, the numbers in the *Misc.* column mean the height, the diameter of the top, and the diameter of the bottom in cm, respectively.

[b] The velocity of this test corresponds to the ejection velocity of the disrupted projectile only, not that of the target ejecta.

## 3. Results and discussions

### 3.1. Maximum ejecta velocity

Figures 1a and 1b show the successive images taken by the image-converter camera. The experimental conditions of Figs. 1a and 1b are $v_i = 650$ m/s, $\phi = 12.5\%$, and $v_i = 646$ m/s, $\phi = 37\%$, respectively. The first image on Figs. 1a and 1b recorded the moment when the projectile contacted the target surface. In the following images, the high-speed fragments ejecting from the impact point can be observed and the ejecta envelope made of the small fragments with the highest velocity in each direction is growing with time. It can be observed clearly that the ejecta envelope of Fig. 1b grows slower than that of Fig. 1a. We analyzed this ejecta envelope by using the same method described in Arakawa et al. (2002) to determine the ejecta angle and the maximum ejecta velocity. The ejecta angles, defined by the angle between the target surface and the direction of the envelope showing the maximum velocity, of Figs. 1a and 1b are almost the same, 39° and 43°, respectively. We observed that the ejecta angle linearly increases from 20° to 50° with the increase of the impact velocity range irrespective of the porosities. The same trend for pure ice found in Arakawa et al. (2002).

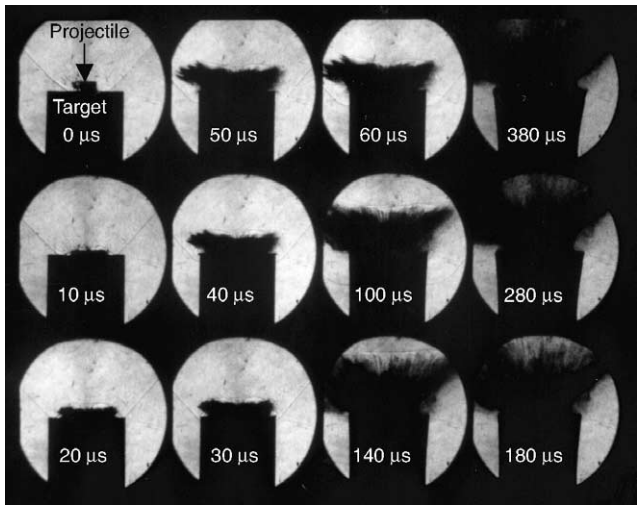


(a)

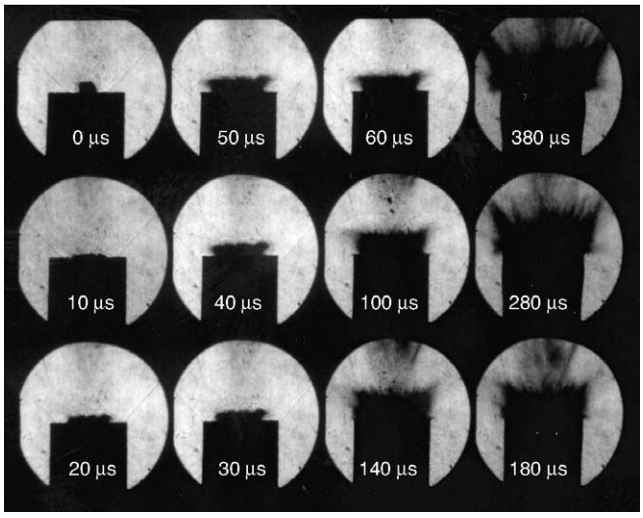


(b)

Fig. 1. (a) Successive images taken by the image converter camera. The experimental condition is $v_i = 650$ m/s and $\phi = 12.5\%$. The numbers in each image are the time after the impact in μs. (b) The images for the experiment of $v_i = 646$ m/s and $\phi = 37\%$.

The maximum ejecta velocity is approximately proportional to the impact velocity for each porosity, the maximum ejecta velocity normalized by the impact velocity is used in our analysis. Figure 2 shows the relationship between the maximum ejecta velocity ($v_{\text{e-max}}/v_i$) and the porosity compared with the previous result of pure ice. The $v_{\text{e-max}}/v_i$ deceases rapidly with increasing porosity: this is an important discovery, i.e., the porous mixture target does not eject high velocity fragments. The maximum velocity of the fragments is slower than half the impact velocity for porosity $> 0.3$. The empirical relationship in Fig. 2 is

$$v_{\text{e-max}}/v_i = -(3.2 \pm 0.4)\phi + (1.4 \pm 0.1). \quad (1)$$

These velocities are slightly below those of pure ice. Both impact experiments used the same ice projectile, so the difference might be due to the target physical properties related

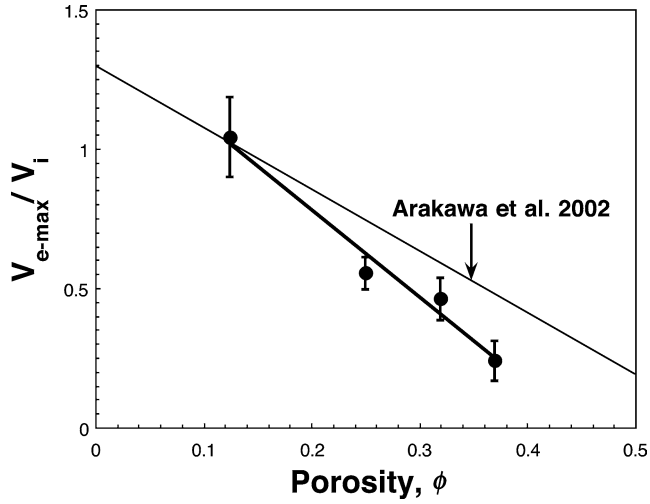


Fig. 2. The maximum ejecta velocity normalized by the impact velocity depending on the target porosity. The error bars mean the standard deviation of the data acquired in each porosity. The previous data of pure ice obtained by Arakawa et al. (2002) is shown for the comparison.

to shock wave propagation, e.g., mean density, bulk sound velocity, and shock pressure attenuation. The ejecta angle and velocity in the crater formation on a non-porous ice–silicate mixture were observed by Koschny and Grün (2001). They used the target containing silicates of 5, 10, and 20% and the crater was made at the velocity ranging from 0.9 to 11.4 km/s. The maximum ejecta velocity was observed to be several 100 m/s independence on the projectile velocity and the maximum velocity appeared at the ejecta angle of 60° to 65°. The cratering experiments on the non-porous ice–silicate mixtures to observe impact ejecta were also conducted by Burchell et al. (2003). Since theses studies are different in the impact velocities ($> 1$ km/s) and the projectile materials (glass, nylon, ceramic, Al, etc.), the difference in the obtained results might be caused by these impact conditions.

### 3.2. Impact strength

The impact strength is usually estimated from the relationship between the largest fragment mass normalized by the initial target mass ($m_l/M_t$) and the energy density, $Q$, which is defined as the kinetic energy of the projectile divided by the target mass (this parameter is the most widely-used parameter to describe the degree of impact). Figure 3a shows all of the results for the target with the silicate content of 50 wt%. The results for 37% porosity are well below the other data, which means that the most porous target is the weakest. The data for porosities from 0 to 32% are almost on the same line, although the non-porous target lies slightly higher. Therefore, it is difficult to distinguish the impact strength among theses targets in terms of $m_l/M_t$.

We have found a large difference on the relationship of $m_l/M_t$ vs. $Q$ between serpentine and pyrophyllite targets with the porosity of 37% as shown in Fig. 3b. Both targets

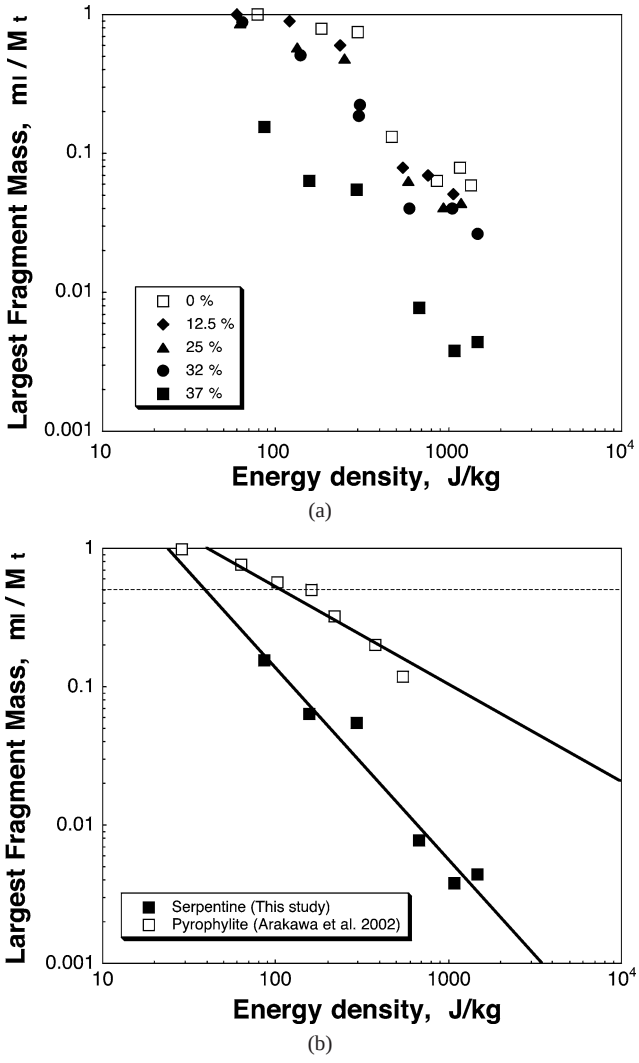


Fig. 3. (a) $m_l/M_t$ vs. energy density for mixture target ($C = 0.5$) with various porosities. (b) Comparison of the impact strength between serpentine and pyrophyllite mixtures. Both samples had the same silicate content of $C = 0.5$ and porosity of $\sim 37\%$. Pyrophyllite data refer to Arakawa et al. (2002). The broken line shows $m_l/M_t = 0.5$, which means a criterion of catastrophic disruption to determine $Q^*$.

have almost the same porosity and silicate-content. However our new results for serpentine clearly shows that it is rather weaker than the target including pyrophyllite. The impact strength ($Q^*$) is widely defined as the energy density which corresponds to $m_l/M_t = 0.5$ (Davis and Ryan, 1990). Thus $Q^*$ is estimated to be 40 and 100 J/kg for serpentine and pyrophyllite mixtures, respectively. Why the serpentine mixture is about twice as weak as the pyrophyllite mixture is not clear. However, the difference of physical properties such as mechanical strength and powder grain size might be responsible for this clear result.

In order to distinguish the confused results of the porosities from 0 to 32% in Fig. 3a, the impact strength can be represented by the parameter $f_{0.5}$ derived from the cumulative mass distribution for each recovered target (Figs. 4a and 4b). This parameter is the fragment mass normalized by the initial target mass that corresponds to half of the initial target mass in the cumulative mass distribution. Hence, a lower value of $f_{0.5}$ means a larger degree of impact disruption. Figures 4a and 4b show the cumulative mass distribution measured for $\phi = 25\%$ and $\phi = 37\%$, respectively; the cross points showing $f_{0.5}$ are illustrated by open circles. These cumulative mass distributions have a notable characteristic in the range of the small fragment mass. All of the distributions are almost constants in that small range and the constants of each cumulative mass are in the order of the impact velocity. This means that the number of fragments ranging from $10^{-5}$ to $10^{-3}$ is relatively small and the mass of the fragments smaller than $10^{-5}$ was generated proportional to the impact velocity. In cases of non-porous ice and rock, it is well known that the cumulative mass increases according to the relationship of a power law in small range of the fragment mass. Therefore, the observed property in Figs. 4a and 4b is considered to be a special feature of porous ice–silicate mixture. In the case of porous sintering targets, we can expect them to break mostly into fragments that are equal to or larger than the original constituents because it is easier to break the bonds between the particles than to break the particles themselves. This could be a main reason to make the special feature of porous targets.

The relationship between $f_{0.5}$ and the energy density, $Q$, is shown in Fig. 5. As seen in Fig. 5, the data for each porosity has a good correlation with the energy density and it can be fit by the empirical power law equations

$$f_{0.5} = q_0 Q^p. \tag{2}$$

The calculated parameters, $q_0$ and $p$, for each porosity data are shown in Table 2. The data at 37% porosity is unique. We observed that the cumulative mass distribution of the 37% porous target is distinctive from others in that more than half of the initial target was disrupted into ice and serpentine particles whit sizes less than 710 μm, which means targets broke into the individual particles with the initial size before pressure sintering (Fig. 4b).

The impact strength, $Q^*_{0.5}$, is defined by the energy density where each empirical equation crosses $f_{0.5} = 0.5$ (Fig. 5). The derived $Q^*_{0.5}$ is tabulated in Table 2 and shown in Fig. 6 compared with the results obtained for pure ice. It is noticeable that the impact strength of mixture decreases with increasing porosity: the strength becomes about a half of the strength of non-porous sample. This trend is completely opposite to that obtained for pure ice. The impact strength of pure ice monotonically increases with increasing porosity. This is the same trend found in other geological materials, e.g., crushed ice aggregates (Ryan et al., 1999), gypsum and clay (Davis and Ryan, 1990), and sintered glass particles (Love et al., 1993). Arakawa et al. (2002) speculated that the porosity dependence of the impact strength of ice–silicate mixtures is opposite to that of pure ice. But that speculation was based on only a few data points. The current more-detailed study of ice–silicate mixtures confirms

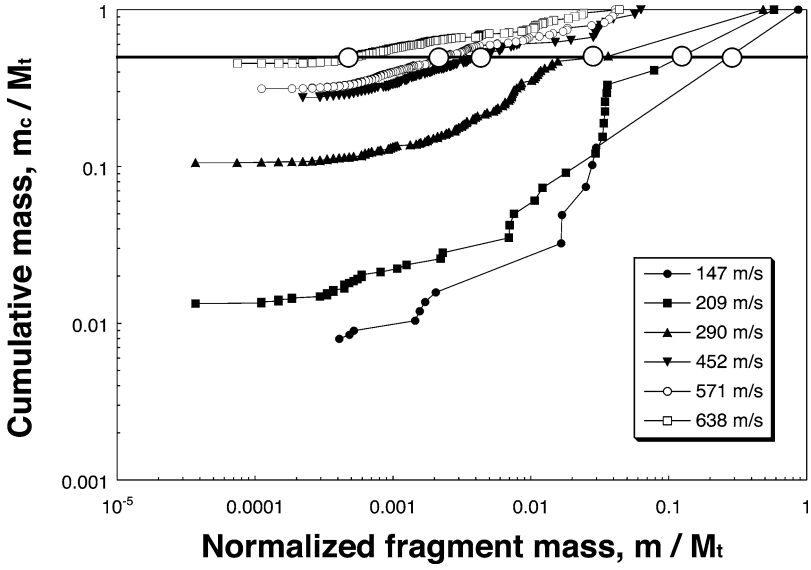


(a)

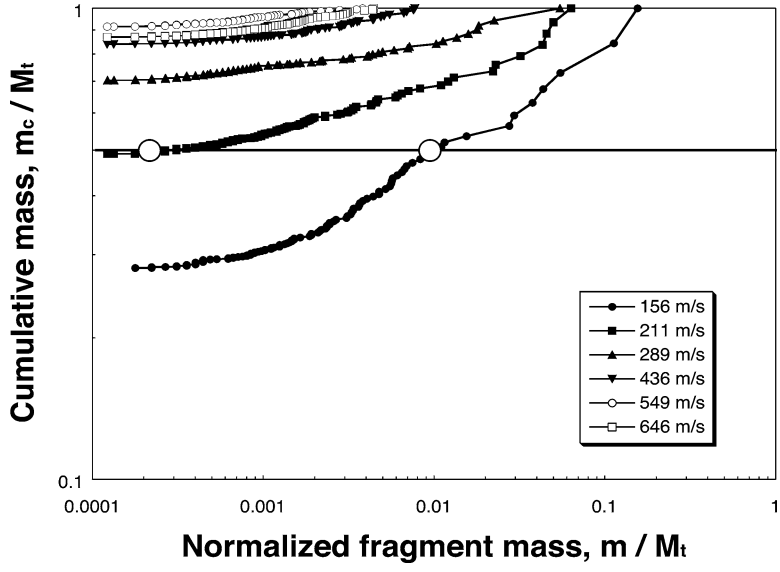


(b)

Fig. 4. (a) Cumulative mass distribution constructed from the recovered fragments for the porous mixture $\phi = 25\%$. $m_c/M_t = 0.5$ is shown in the figure and the cross points on each distribution with $m_c/M_t = 0.5$ are shown as open circles. $m/M_t$ at these cross points are defined as $f_{0.5}$. (b) Cumulative mass distribution constructed from the recovered fragments for the porous mixture $\phi = 37\%$.

the curious trend found previously. The empirical relationship derived for our mixed sample is as follows:

$$Q^*_{0.5} = 124(1-\phi)^{2.5}. \quad (3)$$

Previous results for the pyrophyllite mixture are also plotted on Fig. 6. It is surprising that the data for pyrophyllite is consistent with Eq. (3) although $Q^*$ for the target with the porosity of 37% is quite different as shown in Fig. 3b.

Figure 7 shows the cumulative mass distributions obtained for a series of experiments with various silicate contents including the pure ice data of Arakawa et al. (2002). All of the experiments represented in Fig. 7 had almost the same energy density (230–290 J/kg). It is obvious that the largest fragment mass normalized by the initial target mass is nearly independent of silicate content for $C = 0.1$ to 0.5. Although $f_{0.5}$ is more reliable parameter than the largest fragment mass to estimate the degree of impact disruption, in this case $f_{0.5}$ shows almost no dependence on silicate content. However, the cumulative mass distributions are quite differ-

Table 2
Calculated parameters in Eq. (2) and $Q^*_{0.5}$

| $\phi$ | $q_0$ | $p$ | $Q^*_{0.5}$ (J/kg) |
|---|---|---|---|
| 0 | 4554 | −1.90 | 121.3 |
| 0.125 | 12761 | −2.24 | 92.8 |
| 0.25 | 1878 | −2.05 | 55.4 |
| 0.32 | 2217 | −2.17 | 48.0 |

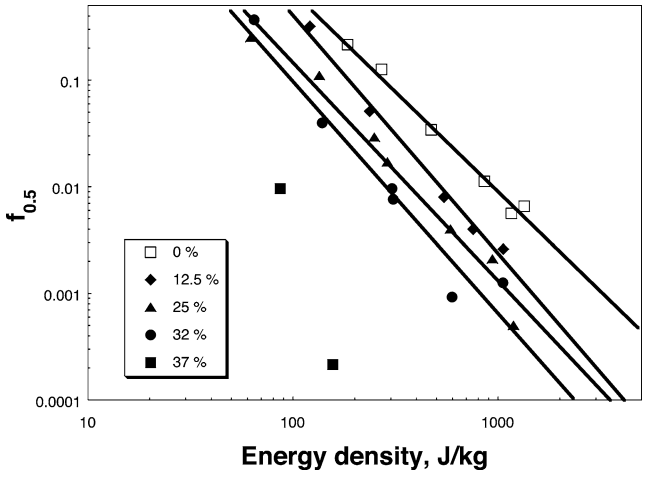


Fig. 5. The relationship between $f_{0.5}$ and energy density. Each line was fit by least square method. The number in the legend with the unit of % shows the sample porosity.

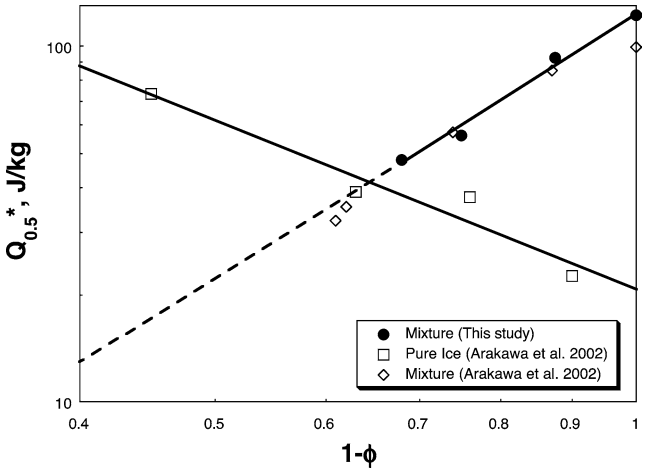


Fig. 6. The impact strength descried by $Q^*_{0.5}$ depending on the target porosity. The line was fit by least square method for the ice–serpentine mixture in this study. The strength data of pyrophyllite mixture derived from Arakawa et al. (2002) was also shown as a symbol of open diamond. The open square symbol is the data for pure ice obtained by Arakawa et al. (2002), the line is showing Eq. (3) in Arakawa et al.

ent from each other in the range of the normalized fragment masses smaller than 0.01. The distributions arrange bottom to top in the order of silicate contents from 0.5 to 0.1. This observation means that the silicate content affects the formation of impact fragments especially around the impact point because small fragments are generated near the impact site, which the shock pressures are high (Melosh, 1989). Hence $f_{0.5}$ is not a sufficient description of the degree of impact disruption. Future studies should look for an additional parameter to distinguish the feature that appears at the range of small fragments.

The comparison with pure ice shows us that $f_{0.5}$ drastically increases between $C = 0$ and 0.1. Figure 8 shows the relationship between $f_{0.5}$ and $C$ estimated from Fig. 7. The trend described above is more clear in this figure. That is, $f_{0.5}$ drastically increases when a small amount of silicate (less than $C = 0.1$) is included and, then, it becomes almost constant at the wide range of $C$ from 0.1 to 0.5. This results might mean that the impact strength defined as $Q^*_{0.5}$ only changes at the silicate contents from 0 to 0.1 and it becomes almost constant at the range from $C = 0.1$ to 0.5 although confirmation of this idea will have to wait for future study.

### 3.3. Static strength

Figure 9 shows the results of the static mechanical tests. The relationships between the maximum stress, $Y$, and the porosity are shown for pure ice and mixtures. The maximum stress increases with decreasing porosity in both samples, however the slope of the relationship of the mixture is steeper than that of the pure ice. The empirical equations obtained by least square fitting for both samples are written as follows:

$$Y = Y_0(1-\phi)^n, \tag{4}$$

where $Y_0$ and $n$ are 9.8 MPa and 3.4, 9.5 MPa and 6.4 for pure ice and mixture, respectively. The result of pure ice is consistent with the summarized data of Mellor (1975). The static strength of the mixture is always weaker than that of the pure ice although the impact strength of the mixture is always stronger than that of the pure ice in this porosity range.

Davis and Ryan (1990) indicated a power law relation between static strength and impact strength ($Q^*$) for various brittle-material with planetological importance. They obtained $Q^*[\mathrm{erg/cm^3}] = 0.12Y[\mathrm{erg/cm^3}]^{0.84}$ in the consideration including ice, tuff and some rocks. In our results, the mixture target shows a good correlation between $Q^*_{0.5}$ and $Y$, which is as follows (Fig. 10):

$$Q^*_{0.5} = 50.8 \cdot Y^{0.39}, \tag{5}$$

where $Q^*_{0.5}$ and $Y$ are in the dimension of J/kg and MPa, respectively. It is interesting that the impact strength of porous fragile targets has a positive dependence on the static strength, which was the same trend found in Davis and Ryan (1990) for intact brittle materials. On the other hand, the impact strength of porous pure ice decreases with the increase of the static strength. This means that in addition to static strength other factors strongly affect the impact strength of porous pure ice, and the attenuation of shock pressure as pointed out by Arakawa et al. (2002).

### 3.4. Implication for accretion process of icy satellites

If Saturn's subnebula was characterized by chemical heterogeneity in the ratio of ice to silicates, we could apply the present results to speculate the density-size distribution of Saturn's satellites and rings. Satellitesimals would have a large porosity because the pressure sintering was very difficult in these small bodies ($\sim$ 10 km) (Maeno et al., 1993). They could grow in size with time by collisional accretion and the pores in the interior collapsed by the internal

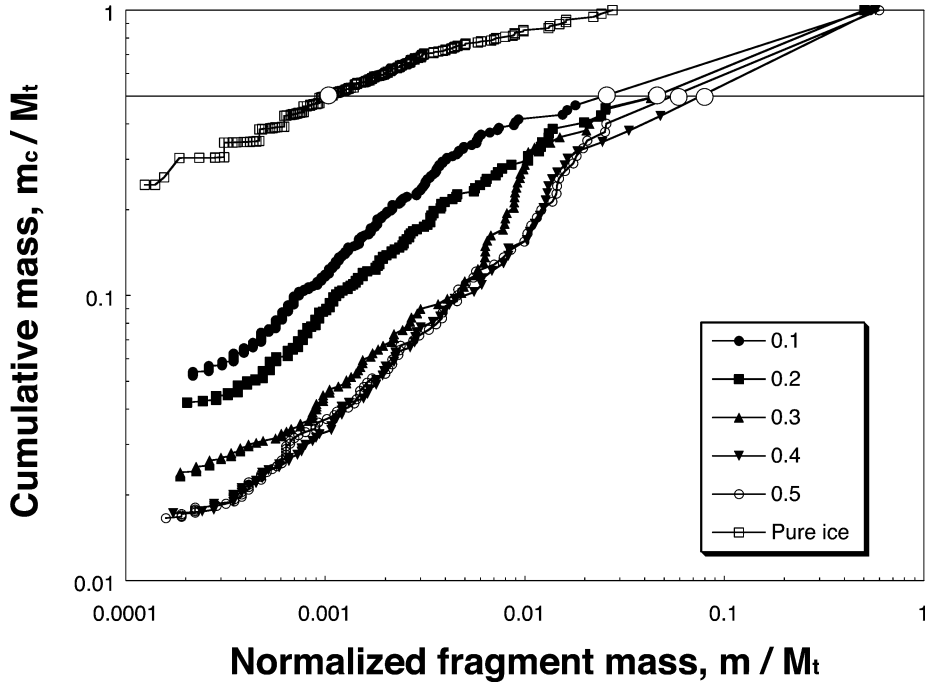


Fig. 7. Cumulative mass distribution for a series of impact experiments with various silicate contents, $C = 0.1$ to 0.5. The number in the legend means the silicate mass ratio, $C$. The data of pure ice comes from Arakawa et al. (2002) for the comparison. The energy densities of the presented data are between 230 and 290 J/kg.

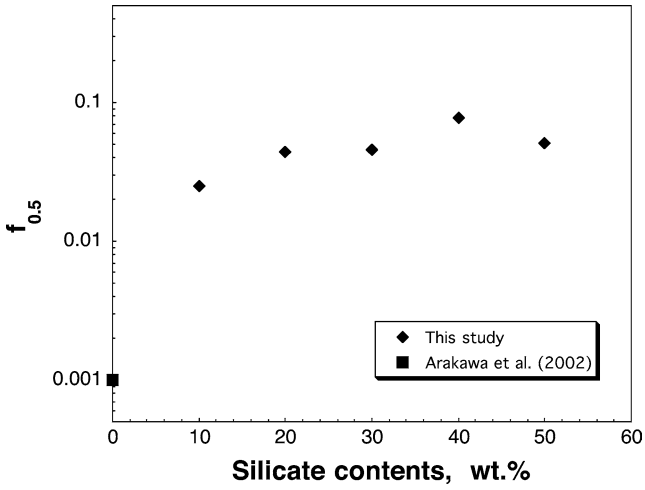


Fig. 8. $f_{0.5}$ vs. silicate contents for mixture targets with the porosity of 12.5%. The plotted data was derived from Fig. 7.

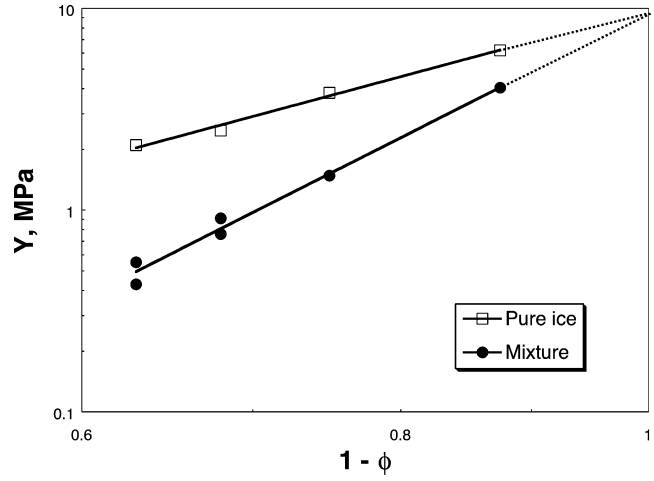


Fig. 9. Static compressive strength of pure ice and mixture depending on the porosities. The maximum stress was measured for unconfined compression tests at the constant strain rate of $5.6 \times 10^{-3}$ s$^{-1}$. Each data is fit by least square method and the results are shown in Eq. (4).

pressure caused by self-gravity. Therefore, a growing body would lose its porosity as it grew and would be completely compacted at the size of about 400 km, which was almost the same as Mimas (Eluszkiewicz, 1990).

We think that the following scenario of ice–silicate fractionation in subnebula might be possible qualitatively. If ice rich bodies were compacted, their low porosity would allow them to be easily disrupted. This mechanism prohibits the growth of the ice rich bodies, and thus these bodies break into small pieces with time. This process might supply ice rich small debris like a constituent of Saturn's rings. On the other hand, compacted silicate rich bodies can withstand collisions, which enhances the growth of silicate rich bodies. This process may be one of the reasons why the larger satellites have larger densities in Saturn's system.

## Acknowledgments

We are grateful to the reviewer, Dr. K. R. Housen, for his very detailed study of the manuscript and his constructive remarks, and we give special thanks to Dr. Ohtsuki of Uni-

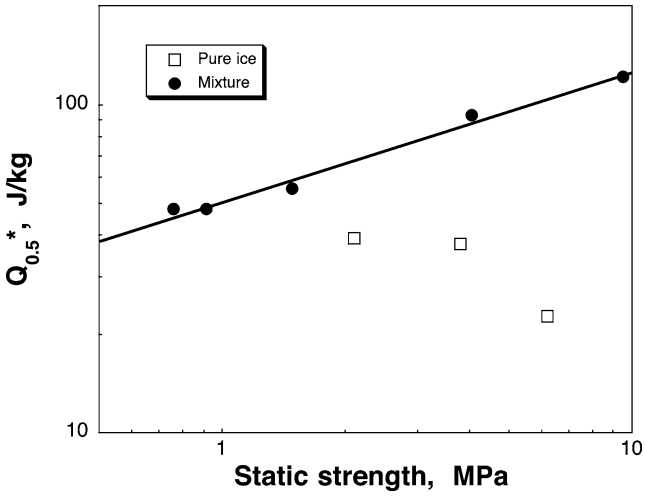


Fig. 10. Correlation between $Q^*_{0.5}$ and static strength for pure ice and mixture ($C = 0.5$) samples. The $Q^*_{0.5}$ data for pure ice refers to Arakawa et al. (2002). The mixture data is fit by a power law equation described in Eq. (5).

versity of Colorado for his useful comments on this paper. We appreciate Prof. Kouchi, Prof. Maeno and Dr. Watanabe of Institute of Low Temperature Science, Hokkaido University for their useful discussions on the experiments. We also thank that S. Nakatsubo, S. Matsumoto, and K. Shinbori of the Contribution Division of Institute of Low Temperature Science, Hokkaido University, for their technical helps. This work was supported by a grant-in-aid for scientific research (Grant 14654082) from the Japan Ministry of Education, Sciences, Sports and Culture.

## References

Ahrens, T.J., O'Keefe, J.D., 1985. Shock vaporization and the accretion of the icy satellites of Jupiter and Saturn. In: Klinger, J., Benest, D., Dollfus, A., Smoluchowski, R. (Eds.), Ices in the Solar System. Reidel, Dordrecht, pp. 631–654.

Arakawa, M., 1999. Collisional disruption of ice by high-velocity impact. Icarus 142, 34–45.

Arakawa, M., Higa, M., 1996. Measurements of ejection velocities in collisional disruption of ice spheres. Planet. Space Sci. 44, 901–908.

Arakawa, M., Maeno, N., Higa, M., Iijima, Y., Kato, K., 1995. Ejection velocity of ice impact fragments. Icarus 118, 341–354.

Arakawa, M., Leliwa-Kopystynski, J., Maeno, N., 2002. Impact experiments on porous icy–silicate cylindrical blocks and the implication for disruption and accumulation of small icy bodies. Icarus 158, 516–531.

Britt, D.T., Consolmagno, G.J., 2001. Modeling the structure of high porosity asteroids. Icarus 152, 134–139.

Burchell, M.J., Galloway, J.A., Bunch, A.W., Brandao, P.F.B., 2003. Survivability of bacteria ejected from icy surfaces after hypervelocity impact. Orig. Life Evol. Biosphere 33, 53–74.

Canup, R.M., Ward, W.R., 2002. Formation of the galilean satellites: conditions of accretion. Astron. J. 124, 3404–3423.

Coradini, A., Cerroni, P., Magni, G., 1989. Formation of the satellites of the outer Solar System: sources of their atmospheres. In: Atreya, S.K., Pollack, J.B., Matthews, M.S. (Eds.), Origin and Evolution of Planetary and Satellite Atmospheres. Univ. of Arizona Press, Tucson, pp. 733–762.

Davis, D.R., Ryan, E.V., 1990. On collisional disruption: experimental results and scaling law. Icarus 83, 156–182.

Eluszkiewicz, J., 1990. Compaction and internal structure of Mimas. Icarus 84, 215–225.

Gladman, B., Nicholson, P., Burns, J.A., Kavelaars, J.J., Marsden, B., Williams, G., Offut, W., 1998. Discovery of two distant irregular moons of Uranus. Nature 392, 897–899.

Gladman, B., Kavelaars, J.J., Holman, M., Petit, J.-M., Scholl, H., Nicholson, P., Burns, J.A., 2000. The discovery of Uranus XIX, XX, and XXI. Icarus 147, 320–324.

Gladman, B., Kavelaars, J.J., Holman, M., Nicholson, P.D., Burns, J.A., Hegenrother, C.W., Petit, J.M., Marsden, B.G., Jacobson, R., Grey, W., Grey, T., 2001. Discovery of 12 satellites of Saturn exhibiting orbiter clustering. Nature 412, 163–166.

Housen, K.R., Holsapple, K.A., 2003. Impacy cratering on porous asteroids. Icarus 163, 102–119.

Housen, K.R., Holsapple, K.A., Voss, M.E., 1999. Compaction as the origin of the unusual craters on the Asteroid Mathilde. Nature 402, 155–157.

Jewitt, D.C., 1999. Kuiper belt objects. Annu. Rev. Earth Planet. Sci. 27, 287–312.

Koschny, D., Grün, E., 2001. Impact into ice–silicate mixtures: ejecta mass and size distributions. Icarus 154, 402–411.

Lange, M.A., Ahrens, T.J., 1983. The dynamic tensile strength of ice and ice–silicate mixtures. J. Geophys. Res. 88, 1197–1208.

Love, S.G., Hörz, F., Brownlee, D.E., 1993. Target porosity effects in impact cratering and collisional disruption. Icarus 105, 216–224.

Lunine, J.I., Stevenson, D.J., 1982. Formation of the galilean satellites in a gaseous nebula. Icarus 52, 14–39.

Lupo, M.J., Lewis, J.S., 1979. Mass-radius relationship in icy satellites. Icarus 40, 157–170.

Luu, J.X., Jewitt, D.C., 2002. Kuiper belt objects: relics from the accretion disk of the Sun. Annu. Rev. Astron. Astrophys. 40, 63–101.

Maeno, N., Arakawa, M., Leliwa-Kopystynski, J., 1993. Deformation of porous ice–rock mixtures and an application to the densification of icy satellites. In: Oya, H. (Ed.), Primitive Solar Nebula and Origin of Planets. Terra Scientific, Tokyo, pp. 341–353.

Mellor, M., 1975. A review of basic snow mechanics. IAHS-AISH Pub. 114, 251–291.

Melosh, H.J., 1989. Impact Cratering. Oxford Univ. Press, Oxford.

Mizutani, H., Takagi, Y., Kawakami, S., 1990. New scaling law on impact fragmentation. Icarus 87, 307–329.

Mosqueria, I., Estrada, P.R., 2003a. Formation of the regular satellites of giant planets in an extended gaseous nebula. I. Subnebula model and accretion of satellites. Icarus 163, 198–231.

Mosqueria, I., Estrada, P.R., 2003b. Formation of the regular satellites of giant planets in an extended gaseous nebula. II. Satellite migration and survival. Icarus 163, 232–255.

Ryan, E.V., Davis, D.R., Giblin, I., 1999. A laboratory impact study of simulated Edgeworth–Kuiper belt objects. Icarus 142, 56–62.